

DETC2017-67633

MESOSCALE MULTI-PHYSICS SIMULATION OF SOLIDIFICATION IN SELECTIVE LASER MELTING PROCESS USING A PHASE FIELD AND THERMAL LATTICE BOLTZMANN MODEL

Dehao Liu

Woodruff School of Mechanical Engineering
Georgia Institute of Technology
Atlanta, GA 30332, USA
dehao.liu@gatech.edu

Yan Wang

Woodruff School of Mechanical Engineering
Georgia Institute of Technology
Atlanta, GA 30332, USA
yan.wang@me.gatech.edu

ABSTRACT

Selective laser melting (SLM) is a powder bed based additive manufacturing process by melting fine-grained metallic powders with a laser heating source. Understanding the solidification of alloys during SLM process is of importance for accurate prediction of microstructures and properties for process design and optimization. In this study, a multi-physics model is developed to simulate evolution of alloy microstructure during solidification, which incorporates heat transfer, fluid dynamics, kinetics of phase transformations, and grain growth. In this integrated simulation framework, the phase field method for the dendritic growth of a dilute binary alloy is coupled with the thermal lattice Boltzmann method for the melt flow and heat transfer. The effects of latent heat, melt flow and cooling rate on solidification process are also investigated. The multi-physics simulation results provide new insight to predict the complex solidification process more accurately than single-physics approaches.

1. INTRODUCTION

Solidification is one of the most important processes to understand and control the build quality in additive manufacturing (AM), such as in selective laser melting (SLM) and fused deposition modelling (FDM). It is a micro-scale phenomenon that involves complicated processes. It begins with the formation of stable nuclei and proceeds into an undercooled melt because of the movement of a liquid–solid interface. During the solidification, the diffusion of the solute, melt convection, motion of the solid phase, and their couplings play important roles in the formation of the microstructure. The solidified microstructure determines the mechanical, thermal, transport, and other properties of the AM product. Therefore,

understanding solidification and control the process are of great interest for scalable AM production.

Among various simulation models, phase field method (PFM) is widely acknowledged to be a versatile and accurate numerical tool to simulate solidification [1–6]. The main advantage of PFM is its simplicity in treating morphological changes of the microstructure. A continuous variable, called the phase field or order parameter ϕ , is used to distinguish between the liquid and solid phases. The interface has a finite thickness, along which ϕ varies gradually. Instead of explicitly tracking the interface, the changes of the microstructure are described by the time evolution of the order parameter ϕ . PFM can be used to simulate phenomena such as eutectic, eutectoid, and dendrite growth in three-dimensional (3D) domain. The latest PFM development incorporated other physical modules and can handle complicated phase transition of multicomponent multiphase alloys, with the consideration of solute diffusion, advection, strain effects, and plastic activity [3,5,7–13]. Recently PFM was used to simulate the microstructure evolution in the powder-bed electron beam additive manufacturing process [14,15]. It was revealed that the greater the undercooling is, the faster the dendrite grows. Increased temperature gradient and the beam scan speed will decrease the columnar dendritic spacing and width of dendrites. However, in the above work, the effects of latent heat and advection of melt flow were not considered.

The influence of melt convection is critical for the formation of solidification microstructures. For example, in directional solidification, the dendrite arm spacing, growth rate, and dendritic morphology are largely changed by natural convection because of gravity and forced convection because of melt flow. Among the methods to simulate fluid flow, lattice Boltzmann method (LBM) has computational advantages over conventional finite volume approaches to solve the Navier–Stokes equations,

especially with complex boundaries [16–18]. LBM is efficient for simulating single-phase and multiphase flows with complex boundary conditions and multiphase interfaces. Unlike conventional numerical schemes based on discretization of macroscopic continuum equations, LBM relies on micro- and mesoscopic kinetic models to simulate physical processes so that the homogenized or averaged properties are consistent with the macroscopic equations. The 3D thermal lattice Boltzmann method has been adopted to simulate the evolution of temperature and velocity field in electron beam melting processes [19]. However, thermal lattice Boltzmann method alone cannot simulate the evolution of dendrite structure, which makes it lack fine grained details.

PFM and LBM have been combined to simulate the dendritic growth in solidification of pure metals and alloys [20–24]. The combination allows for the interplay between solidification and melt flow. Combined 3D PFM and LBM was used to simulate the dendrite growth in a melt flow of Al-3wt%Cu alloy [25]. However, existing PFM and LBM combinations typically adopt isothermal assumption or 1D temperature field [26], which oversimplifies the physical processes. During the rapid solidification in AM processes, the temperature field could be much more complex than the solidification under equilibrium conditions. The release of latent heat during solidification and advection of melt flow will also constantly change the temperature distribution. Therefore, the effect of heat transfer should be included in multi-physics modeling for accurate prediction.

In this study, a multi-physics model that integrates phase field and thermal lattice Boltzmann methods (PF-TLBM) is developed to simulate solidification, in which the diffusion of the solute, melt convection, motion of the solid phase, and heat transfer with latent heat are coupled simultaneously. It is the first time that phase field and thermal lattice Boltzmann methods are ever combined to predict the complex process of solidification. The preliminary simulation results from 2D models in this paper demonstrate the unique effects of latent heat and melt flow on solidification process.

In the remainder of this paper, Section 2 describes the formulation of the proposed PF-TLBM model. Section 3 contains the simulation results of the dendrite growth of a single grain from a liquid under different thermal and flow conditions. And Section 4 provides brief discussions and conclusions.

2. FORMULATION OF THE PROPOSED PF-TLBM MODEL

In this section, the formulation of the proposed PF-TLBM model is described. It includes both aspects of phase field and thermal lattice Boltzmann methods. In addition, the motion of the grain is modeled. The algorithm of PF-TLBM simulation is given.

2.1 Phase Field Method

Similar to multi-phase field methods described in [5,6,27], multi-phase multi-component systems are considered in this work. One of the essential components in PFM is to define a free

energy functional that can describe the physics of phase transition. The free energy functional consists of the interfacial free energy and chemical free energy and is generally defined as

$$F = \int_{\Omega} (f^{GB} + f^{CH}) dV \quad (1)$$

where f^{GB} and f^{CH} are densities of interfacial and chemical free energies respectively within domain Ω . Other terms such as elastic, magnetic, and electric energy may be added depending on the physical problem.

In solidification, the phase field ϕ represents the fraction of solid phase at a location. The fraction of the liquid phase is $\phi_l = 1 - \phi$. The interfacial free energy density is given by

$$f^{GB} = \frac{4\sigma(\mathbf{n})}{\eta} \left\{ |\nabla\phi|^2 + \frac{\pi^2}{\eta^2} \phi(1-\phi) \right\} \quad (2)$$

where $\sigma(\mathbf{n})$ is the anisotropic surface energy, η is the width of the interface between two phases, $\mathbf{n} = \nabla\phi/|\nabla\phi|$ is the local normal to the interface. Preferential growth along principal axes is ensured by setting the anisotropy surface energy in the form of

$$\sigma = \sigma_0 (1 - 3\varepsilon + 4\varepsilon(n_x^4 + n_y^4 + n_z^4)) \quad (3)$$

where ε is the strength of the anisotropy.

The chemical free energy is built from bulk free energies of the individual phases as

$$f^{CH} = h(\phi) f_s(C_s) + h(1-\phi) f_l(C_l) + \mu(C - (\phi_s C_s + \phi_l C_l)) \quad (4)$$

where C is the overall concentration of the solute, and $f_s(C_s)$ and $f_l(C_l)$ are the chemical bulk free energy densities of the solid and liquid phases respectively, μ is the generalized chemical potential or diffusion potential of solute introduced as a Lagrange multiplier to conserve the solute mass balance between the phases. The weight function h is given by

$$h(\phi) = \frac{1}{4} [(2\phi - 1) \sqrt{\phi(1-\phi)} + \frac{1}{2} \arcsin(2\phi - 1)] \quad (5)$$

The kinetic equations for the phase field and concentration variables are

$$\dot{\phi} + \mathbf{u}_s \cdot \nabla\phi = M_{\phi} \left\{ \sigma(\mathbf{n}) \left[\nabla^2\phi + \frac{\pi^2}{\eta^2} \left(\phi - \frac{1}{2} \right) \right] + \frac{\pi}{\eta} \sqrt{\phi(1-\phi)} \Delta G \right\} \quad (6)$$

and

$$\dot{C} + \mathbf{u}_l \cdot \nabla((1-\phi)C_l) + \mathbf{u}_s \cdot \nabla(\phi C_s) = \nabla \cdot (D_l(1-\phi)\nabla C_l) + \nabla \cdot \mathbf{j}_{ar} \quad (7)$$

respectively, where M_{ϕ} is the interface mobility, D_l is the diffusion coefficient in the liquid, \mathbf{u}_l is the velocity of the liquid phase, and \mathbf{u}_s is of the solid phase. At the right-hand side of Eq. (7), the anti-trapping current is expressed as

$$\mathbf{j}_{ar} = \frac{\eta}{\pi} \sqrt{\phi(1-\phi)} (C_l - C_s) \dot{\phi} \frac{\nabla\phi}{|\nabla\phi|} \quad (8)$$

which is necessary to eliminate the effect of numerical solute trapping because of the diffusion of the interface.

In order to calculate the concentration of liquid and solid phases during solidification, a linear phase diagram is adopted with the constant partition coefficient $k = C_s / C_l$. The driving force is given by $\Delta G = \Delta S(T_m - T + m_l C_l)$, where ΔS is the entropy difference between phases, T_m is the melting temperature of a pure substance, and m_l is the liquidus slope. The advections of the phase field ϕ and concentration C are calculated by the upwind method.

2.2 Thermal Lattice Boltzmann Method

To simulate the melt flow and heat transfer simultaneously, thermal lattice Boltzmann method (TLBM) [18,28–34] is applied. The continuum equations for melt flow and heat transfer are given by

$$\nabla \cdot \mathbf{u}_l = 0 \quad (9)$$

$$\frac{\partial}{\partial t}(\phi \mathbf{u}_l) + \nabla \cdot (\phi \mathbf{u}_l \mathbf{u}_l) = -\frac{\phi}{\rho} \nabla P + \nabla \cdot [\nu \nabla (\phi \mathbf{u}_l)] + \mathbf{F}_d \quad (10)$$

$$\frac{\partial T}{\partial t} + \nabla \cdot (\mathbf{u}_l T) = \nabla \cdot (\alpha \nabla T) + q \quad (11)$$

with the liquid density ρ , pressure P , kinematic viscosity ν , force source term \mathbf{F}_d , temperature T , thermal diffusivity α , and heat source term q .

In order to specify the force and heat source terms, the latent heat caused by solidification is given by

$$q = \frac{L_H}{c_p} \frac{\partial \phi}{\partial t} \quad (12)$$

where L_H is the latent heat of fusion, and c_p is the specific heat of capacity. The dissipative force because of the interaction between solid and liquid phases is

$$\mathbf{F}_d = -h^* (1 - \phi) \rho \nu \frac{\phi^2}{\eta^2} (\mathbf{u}_l - \mathbf{u}_s) \quad (13)$$

where $h^* = 147$ is the numerical coefficient fitted from the calculation of Poiseuille flow in a channel with diffuse walls [22]. The dissipative force is caused by the friction between liquid and solid, which guarantees a no-slip condition with the thin-interface limit.

In TLBM, two particle distribution functions $f_i(\mathbf{x}, t)$ and $g_i(\mathbf{x}, t)$ represent the density and temperature distributions respectively in the i^{th} direction in a regular spatial lattice. The index i corresponds to a unique direction in the lattice, where the corresponding velocity \mathbf{e}_i is also differentiated. For instance, in a two-dimensional D2Q9 model where each node has eight neighbors, the velocity vector \mathbf{e}_i is defined as

$$\mathbf{e}_i = \begin{cases} (0, 0), & i = 0 \\ (\pm c, 0), (0, \pm c), & i = 1, \dots, 4 \\ (\pm c, \pm c), & i = 5, \dots, 8 \end{cases} \quad (14)$$

where $c = \Delta x / \Delta t$ is the lattice velocity with spatial resolution Δx and time step Δt .

The macroscopic quantities of density, velocity, and temperature are calculated from f_i 's and g_i 's as

$$\rho = \sum_i f_i \quad (15)$$

$$\rho \mathbf{u}_l = \sum_i \mathbf{e}_i f_i + \frac{\Delta t}{2} \mathbf{F}_d \quad (16)$$

$$T = \sum_i g_i + \frac{\Delta t}{2} q \quad (17)$$

respectively. The evolutions of f_i and g_i are modeled by

$$f_i(\mathbf{x} + \mathbf{e}_i \Delta t, t + \Delta t) - f_i(\mathbf{x}, t) = \frac{1}{\tau_f} (f_i^{eq}(\mathbf{x}, t) - f_i(\mathbf{x}, t)) + F_i(\mathbf{x}, t) \Delta t \quad (18)$$

and

$$g_i(\mathbf{x} + \mathbf{e}_i \Delta t, t + \Delta t) - g_i(\mathbf{x}, t) = \frac{1}{\tau_g} (g_i^{eq}(\mathbf{x}, t) - g_i(\mathbf{x}, t)) + Q_i(\mathbf{x}, t) \Delta t \quad (19)$$

with dimensionless relaxation time parameters τ_f and τ_g respectively. The force source term and heat source term in the forcing scheme are given as [33,35]

$$F_i = \left(1 - \frac{1}{2\tau_f}\right) \omega_i \left(\frac{\mathbf{e}_i \cdot \mathbf{u}_l}{c_s^2} + \frac{\mathbf{e}_i \cdot \mathbf{u}_l}{c_s^4} \mathbf{e}_i \right) \cdot \mathbf{F}_d \quad (20)$$

and

$$Q_i = \left(1 - \frac{1}{2\tau_g}\right) \omega_i q \quad (21)$$

respectively. The equilibrium distributions $f_i^{eq}(\mathbf{x}, t)$ and $g_i^{eq}(\mathbf{x}, t)$ are given by

$$f_i^{eq}(\mathbf{x}, t) = \omega_i \rho \left[1 + \frac{\mathbf{e}_i \cdot \mathbf{u}_l}{c_s^2} + \frac{(\mathbf{e}_i \cdot \mathbf{u}_l)^2}{2c_s^4} - \frac{\mathbf{u}_l^2}{2c_s^2} \right] \quad (22)$$

and

$$g_i^{eq}(\mathbf{x}, t) = \omega_i T \left[1 + \frac{\mathbf{e}_i \cdot \mathbf{u}_l}{c_s^2} + \frac{(\mathbf{e}_i \cdot \mathbf{u}_l)^2}{2c_s^4} - \frac{\mathbf{u}_l^2}{2c_s^2} \right] \quad (23)$$

For the two-dimensional D2Q9 model, the weights ω_i are given by

$$\omega_i = \begin{cases} 4/9, & i = 0 \\ 1/9, & i = 1, \dots, 4 \\ 1/36, & i = 5, \dots, 8 \end{cases} \quad (24)$$

The speed of sound is given by $c_s^2 = c^2 / 3$. The dimensionless relaxation times for velocity τ_f and temperature field τ_g are calculated by

$$\tau_f = \frac{\nu}{c_s^2 \Delta t} + 0.5 \quad (25)$$

and

$$\tau_g = \frac{\alpha}{c_s^2 \Delta t} + 0.5 \quad (26)$$

In order to match PFM and LBM, a uniform grid with the same spatial resolution Δx and time step Δt is used. A bounce-back scheme is adopted to satisfy the no-slip boundary condition at the solid-liquid interface. The anti-bounceback scheme is taken to satisfy the thermal boundary condition [36–38].

2.3 Motion of Grain

In traditional phase field methods, the solid phase is typically assumed to be static. To model the detailed information of grain orientation, a scheme of grain motion [22] needs to be considered, which includes the rigid translation and rotation movement of the grains.

The total force acting on a grain is given by

$$\mathbf{F} = -\sum \mathbf{F}_d \quad (27)$$

whereas the total torque is

$$\mathbf{M} = -\sum (\mathbf{r} - \mathbf{R}_{cm}) \times \mathbf{F}_d \quad (28)$$

where $\mathbf{R}_{cm} = \sum \mathbf{r} \phi(\mathbf{r}) / \sum \phi(\mathbf{r})$ is the radius vector corresponding to the center of the mass of the grain.

The translation of grains is modeled by

$$\dot{\mathbf{R}}_{cm} = \mathbf{U}_{cm}, \dot{\mathbf{U}}_{cm} = \mathbf{F} / m \quad (29)$$

and the rotation is given by

$$\dot{\theta} = \omega, \dot{\omega} = \mathbf{M} / \mathbf{I} \quad (30)$$

where \mathbf{U}_{cm} is the velocity of the center of the mass, θ is the rotation angle of the grain, ω is the angular velocity, $m = \rho \sum \phi(\mathbf{r})$ is the total mass of the grain, and

$\mathbf{I} = \sum \phi(\mathbf{r}) (\mathbf{r} - \mathbf{R}_{cm})^2$ is the moment of the inertia. The local velocity of the grain is calculated by

$$\mathbf{u}_s = \mathbf{U}_{cm} + \omega \times (\mathbf{r} - \mathbf{R}_{cm}) \quad (31)$$

2.4 Concurrent Simulation Algorithm in PF-TLBM

Multiple physical effects are involved in the solidification process. In PF-TLBM, different variables are coupled with each other. The major ones include phase field ϕ , its time derivative $\dot{\phi}$, concentration C , temperature T , velocity of liquid \mathbf{u}_l , and velocity of solid \mathbf{u}_s . The basic algorithm of the PF-TLBM is shown in Fig. 1.

When the simulation starts, parameters are initialized. The concentration in PFM is first updated according to Eq. (7). Then the phase field is updated based on Eq. (6) with the updated

concentration values. The updated value of phase field is then passed to the dissipative force in Eq. (13), which is used for motion of grains. It also updates the total force applied in LBM as in Eq. (20). The temperature and velocities are coupled in TLBM as in Eqs. (22) and (23). The updated velocities are passed to update the phase field and concentration by solving the advection equations. The updated temperature and velocities in TLBM are then used in PFM for the next iteration. The dash lines in Fig. 1 represents the information flows and variable value updates during the simulation.

The algorithm is implemented in C++ programming language and integrated with OpenPhase [39]. The OpenMP shared-memory parallel programming framework [40] is used to accelerate the computation.

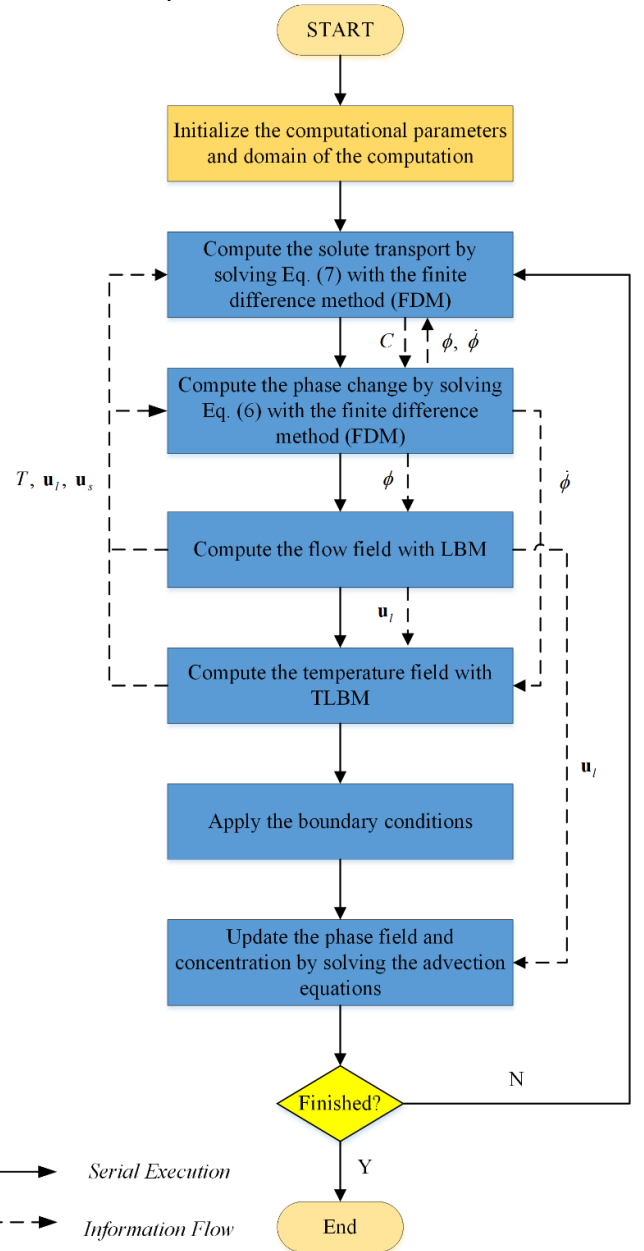


FIGURE 1: Illustration of the flow of execution of the PF-TLBM.

3. SIMULATION RESULTS

The dendrite growth of a single grain from a liquid is simulated under different thermal and flow conditions. Here, aluminum-copper (Al-Cu) is used to demonstrate the simulation scheme. Some physical properties of Al-4wt%Cu alloy are given in Table 1 [22]. In all simulation runs, the grid resolution is $\Delta x = 1 \times 10^{-6}$ m, and the time step is $\Delta t = 2 \times 10^{-7}$ s. The initial temperature is $T = 920$ K, which means that the undercooling is 3.15 K with respect to the initial composition. The length and width of the simulated domain are $L_x = 150 \Delta x$ and $L_y = 150 \Delta x$ in x - and y -directions, respectively. The initial diameter of the seed is $D = 10 \Delta x$, and the width of interface is $\eta = 5 \Delta x$. The initial position of the seed is at the center of the simulation box. The initial concentration of Cu is $C_0 = 4\%$ for the whole computational domain.

TABLE 1: Physical properties of Al-4wt%Cu alloy

Melting point Al	T_m [K]	933.6
Liquidus slope	m_l [K/%]	-2.6
Partition coefficient	k	0.14
Liquid diffusivity	D_l [m ² /s]	3.0×10^{-9}
Interface energy	σ_0 [J/m ²]	0.24
Interface energy anisotropy	ε	0.35
Kinematic viscosity	ν [m ² /s]	5.7×10^{-7}
Thermal diffusivity	α [m ² /s]	4.9×10^{-5}
Latent heat of fusion	L_H [J/kg]	3.98×10^5
Specific heat capacity	c_p [J/(kg·K)]	1450

3.1 Isothermal Dendrite Growth

For comparison purpose, dendrite growth under isothermal condition is first simulated. In initiation, a single grain is created at the center of the simulation box. The system is cooled down with a cooling rate $\dot{T} = 2 \times 10^4$ K/s. For phase field ϕ and concentration C , zero Neumann conditions are set at all boundaries. Adiabatic boundary conditions are set at all boundaries of the temperature field. There is no fluid flow, and the grain is static.

Simulation results are shown in Fig. 2. Because of the symmetric boundary conditions, dendrite growth displays the symmetry about the x -axis. For the convenience of illustration, each picture in Fig. 2 was split into upper and lower parts, corresponding to the concentration and temperature fields respectively.

It is observed that the primary arms of dendrite grow faster than the secondary arms, which shows the anisotropy of the interface energy. Because solid phase has a lower concentration of Cu than liquid phase, the segregation of Cu is observed at the

solid-liquid interface. The temperature keeps the same in the whole simulation domain. However, because of the high cooling rate, there is no large difference between growth rates at different directions of dendrite. The grain grows in a diamond shape. Without considering the effect of latent heat, the temperature was reduced to 120 K at 40 ms, which is far below the room temperature. At the same time, the solidification was not finished in the supercooled liquid and no dendrites were observed, which is not physical and against to the experimental evidence.

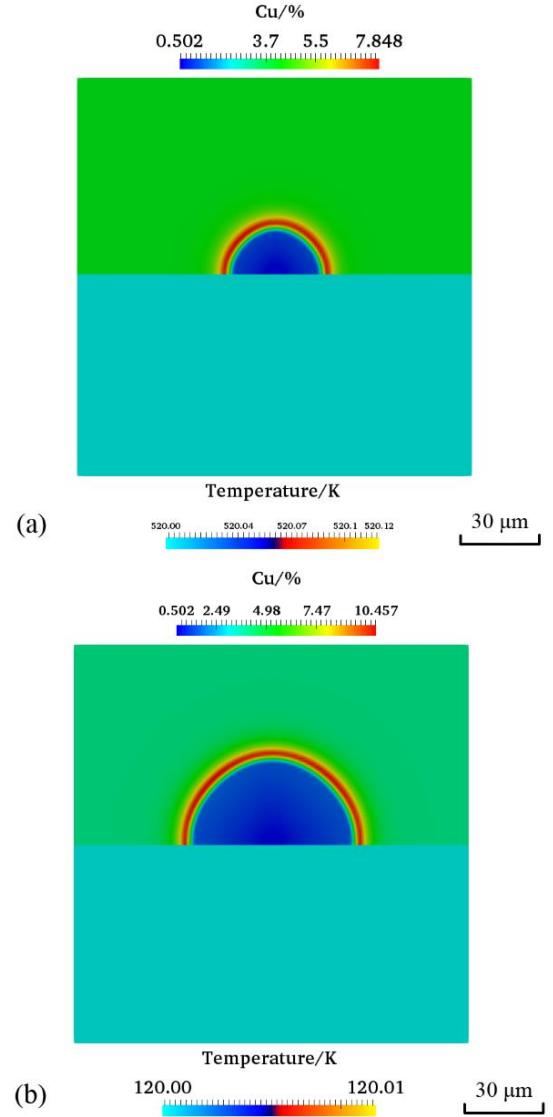


FIGURE 2: Isothermal dendrite growth with a constant cooling rate of $\dot{T} = 2 \times 10^4$ K/s at (a) 20 ms and (b) 40 ms.

3.2 Non-isothermal Dendrite Growth

To simulate the non-isothermal dendrite growth with flow, the release of latent heat during the phase transformation is considered. Given a constant cooling rate $\dot{T} = 2 \times 10^4$ K/s, a fixed heat flux $q_H = \rho c_p \dot{T} L_y / 2$ is set at the upper and lower boundaries, similar to Ref. [9]. For phase field ϕ and

concentration C , zero Neumann conditions are set at all boundaries. Adiabatic boundary conditions are set at the left and

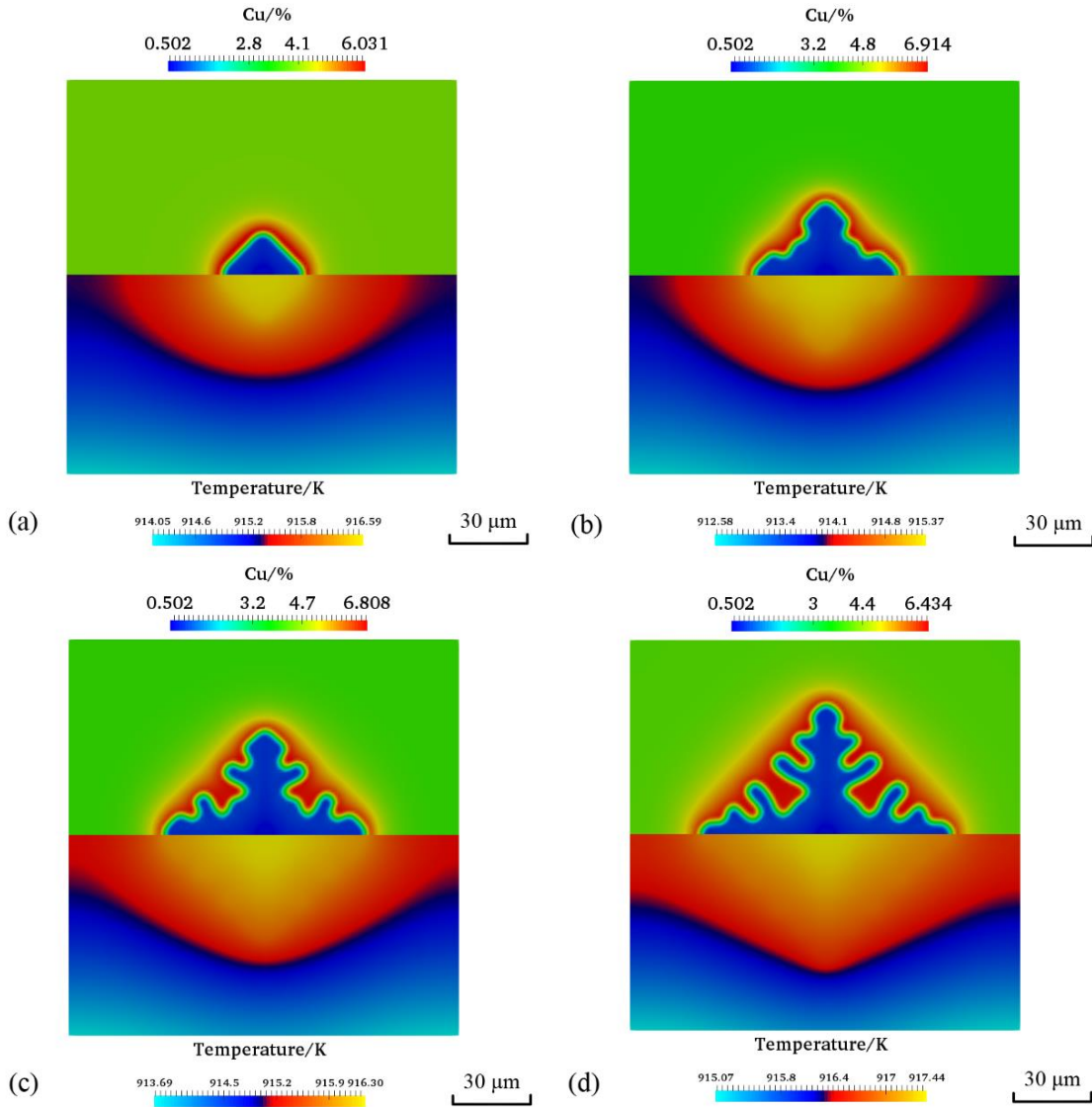


FIGURE 3: Non-isothermal dendrite growth with a fixed heat flux at (a) 25 ms, (b) 50 ms, (c) 75 ms and (d) 100ms.

right boundaries of temperature field. Simulation results are shown in Fig. 3.

Compared to the isothermal dendrite growth, the concentration, temperature distribution, and the pattern of non-isothermal dendrite growth are quite different. Because of the release of latent heat and the delay of heat balance, the temperature of the whole domain is higher than the isothermal case, and the growth rate of dendrite is lower under the non-isothermal condition. The temperature of solid phase is also higher than that of liquid phase, which decreases the undercooling and driving force of growth. The level of Cu segregation at the solid-liquid phase is lower under the non-isothermal case. The grain grows as a dendrite with four-fold symmetry.

The simulation result shows that it is very important to consider the heat transfer during the solidification process, since significant differences of concentration, temperature field, and morphology of the grain growth are observed.

3.3 Non-isothermal Dendrite Growth in a Forced Flow

A further refinement of the model is to incorporate fluid flow effect. A constant flow velocity $u_x = 5 \times 10^{-4}$ m/s is imposed at the upper and lower boundaries of the domain. The boundary conditions for the flow at the left boundary $x = 0$ and right $x = L_x$ are periodic. For phase field ϕ and concentration C , zero Neumann conditions are set at all four boundaries. Given a constant cooling rate $\dot{T} = 2 \times 10^4$ K/s, a

fixed heat flux $q_H = \rho c_p \dot{T}_y / 2$ is set at the upper and lower boundaries, whereas adiabatic boundary conditions are set at the left and right boundaries. Simulation results are shown in Fig. 4.

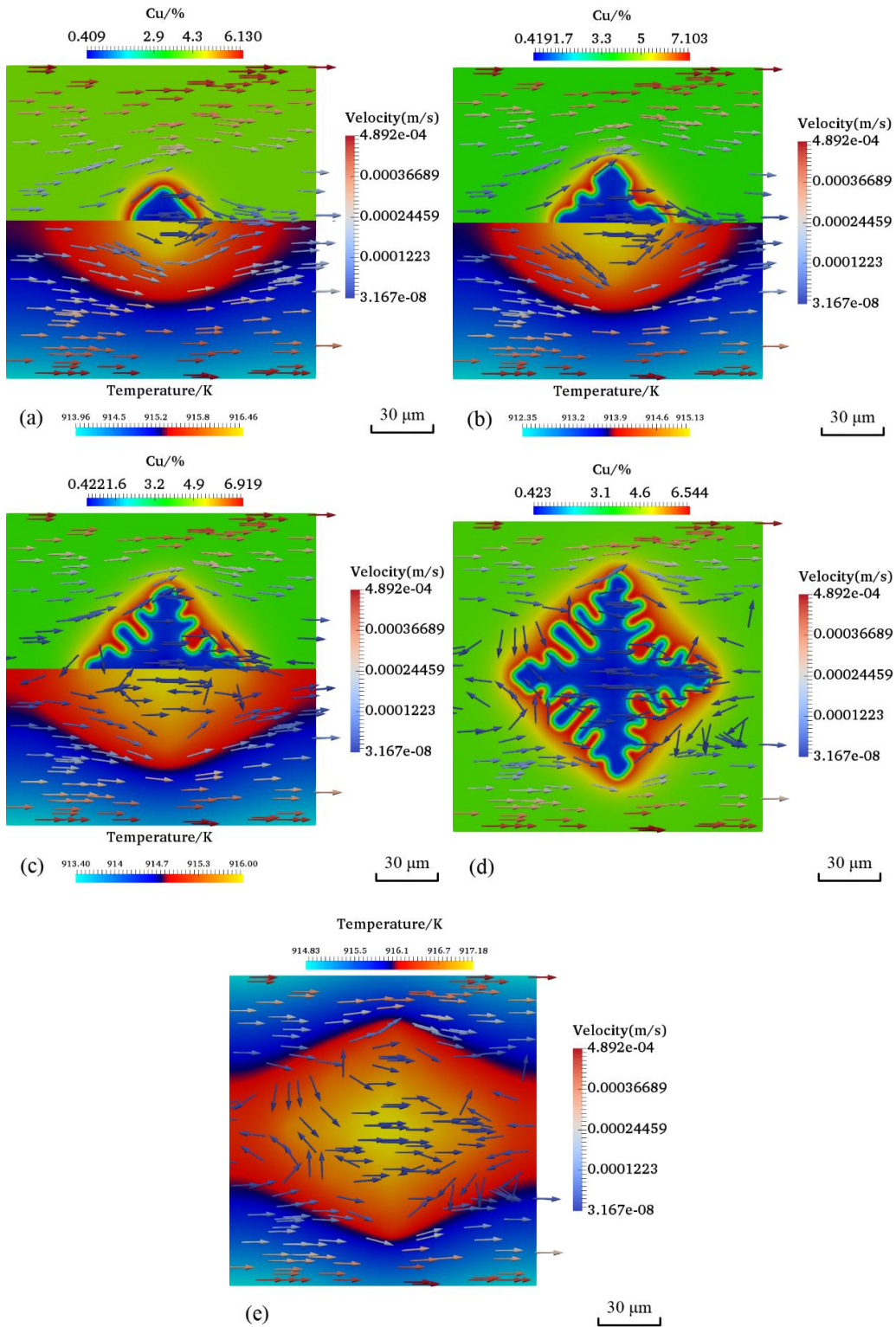


FIGURE 4: Non-isothermal dendrite growth in a forced flow with fixed heat fluxes at (a) 25 ms, (b) 50 ms, (c) 75 ms, (d) concentration and velocity at 100 ms, (e) temperature and velocity at 100 ms.

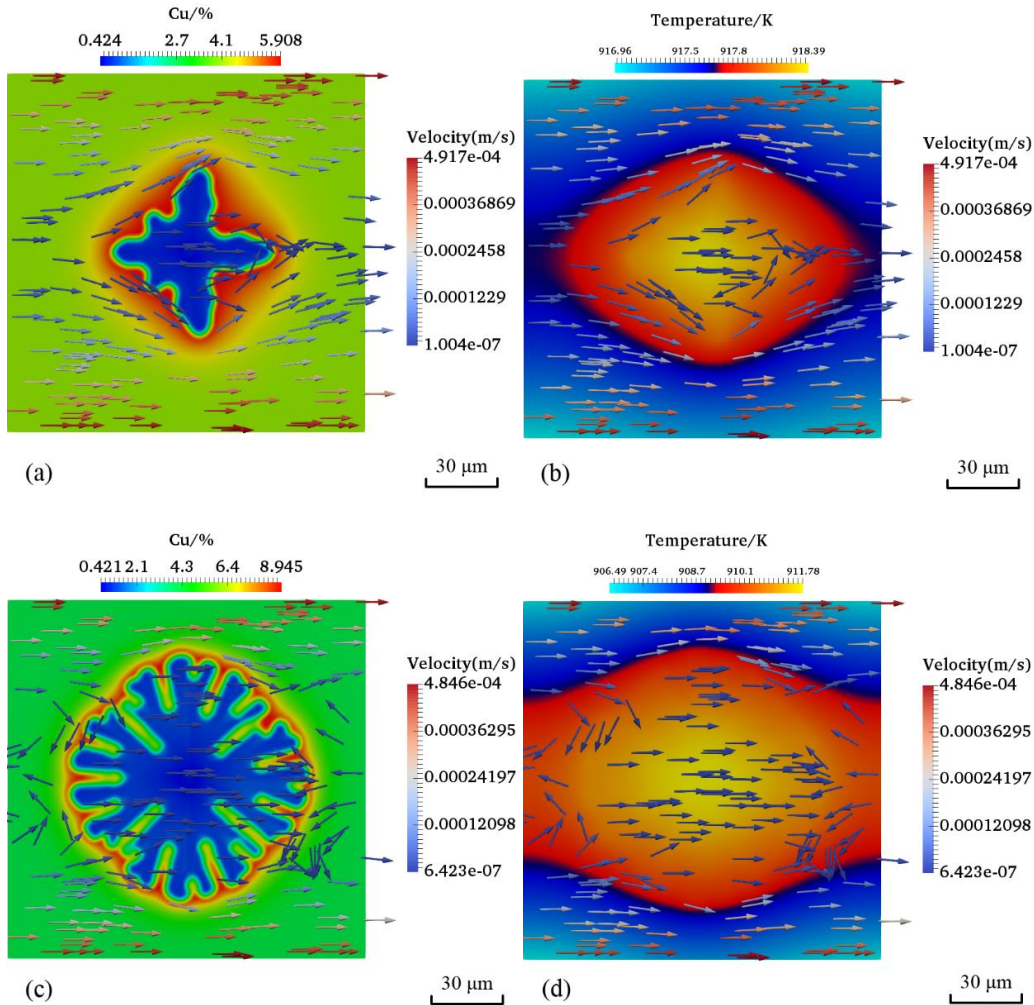


FIGURE 5: Non-isothermal dendrite growth in a forced flow with cooling rates (a) and (b) $\dot{T} = 1 \times 10^4$ K/s at 100 ms, and (c) and (d) $\dot{T} = 5 \times 10^4$ K/s at 75 ms respectively.

It can be seen that the upstream portion of dendrite grows faster than the downstream one since the flow brings fresh material to its vicinity and cools the upstream portion faster, which increases the undercooling. It corresponds to the observation that the temperature gradient at the upstream portion is smaller than the downstream portion. With the effects of the forced flow, the average velocity of the center of dendrite mass reaches 1.0×10^{-5} m/s. Meanwhile, the primary arm against the flow is a little deflected. Some vortexes can be observed around the downstream portion of the dendrites as shown in Figs. 4(d) and (e).

Future work will include the quantitative measurement from both experimental and simulation results for the purpose of model calibration and validation.

3.4 The Effect of Cooling Rate

In order to study the effect of cooling rate, two different cooling rates, $\dot{T} = 1 \times 10^4$ K/s and 5×10^4 K/s, are applied. A fixed heat flux $q_H = \rho c_p \dot{T} L_y / 2$ is set at the upper and lower boundaries similar to Ref. [9]. Other boundary conditions are kept the same as the ones in Section 3.3. Simulation results of $\dot{T} = 1 \times 10^4$ K/s are shown in Figs. 5(a) and (b), whereas the results of $\dot{T} = 5 \times 10^4$ K/s are shown in Figs. 5(c) and (d).

It is seen that with the increase of cooling rate, the growth rate of secondary arms of dendrite increases, which makes the grain grows in a seaweed shape gradually. The growth speed of secondary arms is similar with that of primary arms. A higher cooling rate also results in higher segregation of Cu at the solid-liquid interface. The simulation results show that cooling rate is

a sensitive and important factor which determines the morphology of dendrite growth.

4. DISCUSSIONS AND CONCLUSIONS

A mesoscale multi-physics model is developed to simulate the solidification process in SLM based on phase field and thermal lattice Boltzmann methods. The model incorporates heat transfer, fluid dynamics, kinetics of phase transformation, and grain growth. By considering the heat transfer process, the model can predict the concentration, temperature field, and grain growth pattern in more details than iso-thermal model. The effects of latent heat are also studied. Because of the release of latent heat and the delay of heat balance, the temperature of the domain tends to be higher than the one without latent heat consideration. The growth rate of dendrite is smaller under the non-isothermal condition. The temperature of solid phase is also higher than liquid phase, which decreases the undercooling and driving force of growth.

The advection of melt flow breaks the four-fold symmetry of dendrite growth by changing the distribution of temperature and concentration. The upstream portion of dendrite grows faster than the downstream portion since the flow brings fresh material to its vicinity, which increases the undercooling. Higher cooling rate increases the growth rate of secondary arms of dendrite, which makes the grain grows in a diamond shape gradually.

Our simulation results show that it is important to consider heat transfer, fluid dynamics, kinetics of phase transformations, and grain growth simultaneously in order to provide detailed insight of the physical processes in SLM. Yet, the challenge is to couple multiple physical effects in one single model, particularly with different time scales. In SLM, high cooling rate during rapid solidification needs to be simulated. Therefore, the time step has to be adjusted to be small enough to stabilize the simulation. However, the dimensionless relaxation time in TLBM should be greater than 0.5 for stable simulation, and should not be too large in order to reduce truncation errors [41]. It is ideal for the relaxation time τ_f and τ_g to be both unity.

Although the current model is applied to the 2D conditions for reducing the computation cost, it can be extended to 3D conditions easily. Since TLBM is easy to be parallelized, it can be computationally efficient for large systems. Multi-core processors such as graphical processing units can be employed to increase the simulation speed [25]. This work shows some preliminary results of PF-TLBM. Future work will include the quantitative measurement from both experimental and simulation results for the purpose of model calibration and validation. The model will be used to simulate solidification of different materials used in SLM, including Ti-6Al-4V, stainless steel, and others.

The proposed mesoscale PF-TLBM model is an important component in a multiscale multi-physics simulation framework for SLM processes, where complex boundary conditions need to be considered. It simulates systems at a reasonable time scale for manufacturing processes while providing fine-grained material phase and composition information. Material properties can be

predicted for process design and optimization. Classical continuum simulation schemes do not provide material properties, whereas atomistic models do not simulate the time scales that are long enough for manufacturing processes. Mesoscale simulations fill the gap.

REFERENCES

- [1] Boettinger, W. J., Warren, J. A., Beckermann, C., and Karma, A., 2002, "Phase Field Simulation of Solidification," *Annu. Rev. Mater. Res.*, **32**(1), pp. 63–94.
- [2] Chen, L.-Q., 2002, "Phase-Field Models for Microstructure Evolution," *Annu. Rev. Mater. Res.*, **32**(1), pp. 113–140.
- [3] Singer-Loginova, I., and Singer, H. M., 2008, "The Phase Field Technique for Modeling Multiphase Materials," *Reports Prog. Phys.*, **71**(10), p. 106501.
- [4] Moelans, N., Blanpain, B., and Wollants, P., 2008, "An Introduction to Phase-Field Modeling of Microstructure Evolution," *Calphad Comput. Coupling Phase Diagrams Thermochem.*, **32**(2), pp. 268–294.
- [5] Steinbach, I., 2009, "Phase-Field Models in Materials Science," *Model. Simul. Mater. Sci. Eng.*, **17**(7), p. 73001.
- [6] Steinbach, I., 2013, "Phase-Field Model for Microstructure Evolution at the Mesoscopic Scale," *Annu. Rev. Mater. Res.*, **43**(1), pp. 89–107.
- [7] Beckermann, C., Diepers, H.-J., Steinbach, I., Karma, a, and Tong, X., 1999, "Modeling Melt Convection in Phase-Field Simulations of Solidification," *J. Comput. Phys.*, **154**(2), pp. 468–496.
- [8] Kim, S. G., Kim, W. T., and Suzuki, T., 1999, "Phase-Field Model for Binary Alloys.," *Phys. Rev. E. Stat. Phys. Plasmas. Fluids. Relat. Interdiscip. Topics*, **60**(6 Pt B), pp. 7186–7197.
- [9] Loginova, I., Amberg, G., and Ågren, J., 2001, "Phase-Field Simulations of Non-Isothermal Binary Alloy Solidification," *Acta Mater.*, **49**(4), pp. 573–581.
- [10] Lan, C. W., and Shih, C. J., 2004, "Phase Field Simulation of Non-Isothermal Free Dendritic Growth of a Binary Alloy in a Forced Flow," *J. Cryst. Growth*, **264**(1–3), pp. 472–482.
- [11] Ramirez, J. C., Beckermann, C., Karma, a, and Diepers, H.-J., 2004, "Phase-Field Modeling of Binary Alloy Solidification with Coupled Heat and Solute Diffusion.," *Phys. Rev. E. Stat. Nonlin. Soft Matter Phys.*, **69**(5 Pt 1), p. 51607.
- [12] Nestler, B., Garcke, H., and Stinner, B., 2005, "Multicomponent Alloy Solidification: Phase-Field Modeling and Simulations," *Phys. Rev. E - Stat. Nonlinear, Soft Matter Phys.*, **71**(4), pp. 1–6.
- [13] Steinbach, I., 2013, "Why Solidification? Why Phase-Field?," *Jom*, **65**(9), pp. 1096–1102.
- [14] Gong, X., and Chou, K., 2015, "Phase-Field Modeling of Microstructure Evolution in Electron Beam Additive Manufacturing," *Jom*, **67**(5), pp. 1176–1182.

- [15] Sahoo, S., and Chou, K., 2016, "Phase-Field Simulation of Microstructure Evolution of Ti-6Al-4V in Electron Beam Additive Manufacturing Process," *Addit. Manuf.*, **9**, pp. 14–24.
- [16] Aidun, C. K., Clausen, J. R., and Woodruff, G. W., 2010, "Lattice-Boltzmann Method for Complex Flows," *Annu. Rev. Fluid Mech.*, **42**, pp. 439–72.
- [17] Chen, S., and Doolen, G. D., 1998, "Lattice Boltzmann Method for Fluid Flows," *Annu. Rev. Fluid Mech.*, **84**(Kadanoff 1986), p. 16704.
- [18] Li, Q., Luo, K. H., Kang, Q. J., He, Y. L., Chen, Q., and Liu, Q., 2016, "Lattice Boltzmann Methods for Multiphase Flow and Phase-Change Heat Transfer," *Prog. Energy Combust. Sci.*, **52**, pp. 62–105.
- [19] Ammer, R., Markl, M., Ljungblad, U., Körner, C., and Råde, U., 2014, "Simulating Fast Electron Beam Melting with a Parallel Thermal Free Surface Lattice Boltzmann Method," *Comput. Math. with Appl.*, **67**(2), pp. 318–330.
- [20] Medvedev, D., and Kassner, K., 2005, "Lattice Boltzmann Scheme for Crystal Growth in External Flows," *Phys. Rev. E - Stat. Nonlinear, Soft Matter Phys.*, **72**(5), pp. 1–10.
- [21] Miller, W., Rasin, I., and Succi, S., 2006, "Lattice Boltzmann Phase-Field Modelling of Binary-Alloy Solidification," *Phys. A Stat. Mech. its Appl.*, **362**(1), pp. 78–83.
- [22] Medvedev, D., Varnik, F., and Steinbach, I., 2013, "Simulating Mobile Dendrites in a Flow," *Procedia Comput. Sci.*, **18**, pp. 2512–2520.
- [23] Rojas, R., Takaki, T., and Ohno, M., 2015, "A Phase-Field-Lattice Boltzmann Method for Modeling Motion and Growth of a Dendrite for Binary Alloy Solidification in the Presence of Melt Convection," *J. Comput. Phys.*, **298**, pp. 29–40.
- [24] Takaki, T., Rojas, R., Ohno, M., Shimokawabe, T., and Aoki, T., 2015, "GPU Phase-Field Lattice Boltzmann Simulations of Growth and Motion of a Binary Alloy Dendrite," *IOP Conf. Ser. Mater. Sci. Eng.*, **84**, p. 12066.
- [25] Sakane, S., Takaki, T., Rojas, R., Ohno, M., Shibuta, Y., Shimokawabe, T., and Aoki, T., 2016, "Multi-GPUs Parallel Computation of Dendrite Growth in Forced Convection Using the Phase-Field-Lattice Boltzmann Model," *J. Cryst. Growth*, (xxxx), pp. 1–6.
- [26] Schmitz, G. J., Böttger, B., and Apel, M., 2016, "On the Role of Solidification Modelling in Integrated Computational Materials Engineering 'ICME,'" *IOP Conf. Ser. Mater. Sci. Eng.*, **117**(1), p. 12041.
- [27] Steinbach, I., Pezzolla, F., Nestler, B., Seeßelberg, M., Prieler, R., Schmitz, G. J., and Rezende, J. L. L., 1996, "A Phase Field Concept for Multiphase Systems," *Phys. D Nonlinear Phenom.*, **94**(3), pp. 135–147.
- [28] He, X., Chen, S., and Doolen, G. D., 1998, "A Novel Thermal Model for the Lattice {B}oltzmann Method in Incompressible Limit," *J. Comput. Phys.*, **146**(1), pp. 282–300.
- [29] Chakraborty, S., and Chatterjee, D., 2007, "An Enthalpy-Based Hybrid Lattice-Boltzmann Method for Modelling Solid-liquid Phase Transition in the Presence of Convective Transport," *J. Fluid Mech.*, **592**(2007), pp. 155–175.
- [30] Guo, Z., Zheng, C., Shi, B., and Zhao, T. S., 2007, "Thermal Lattice Boltzmann Equation for Low Mach Number Flows: Decoupling Model," *Phys. Rev. E - Stat. Nonlinear, Soft Matter Phys.*, **75**(3), pp. 1–15.
- [31] Attar, E., and Körner, C., 2011, "Lattice Boltzmann Model for Thermal Free Surface Flows with Liquid-Solid Phase Transition," *Int. J. Heat Fluid Flow*, **32**(1), pp. 156–163.
- [32] Eshraghi, M., and Felicelli, S. D., 2012, "An Implicit Lattice Boltzmann Model for Heat Conduction with Phase Change," *Int. J. Heat Mass Transf.*, **55**(9–10), pp. 2420–2428.
- [33] Seta, T., 2013, "Implicit Temperature-Correction-Based Immersed-Boundary Thermal Lattice Boltzmann Method for the Simulation of Natural Convection," *Phys. Rev. E - Stat. Nonlinear, Soft Matter Phys.*, **87**(6), pp. 1–16.
- [34] Perumal, D. A., and Dass, A. K., 2015, "A Review on the Development of Lattice Boltzmann Computation of Macro Fluid Flows and Heat Transfer," *Alexandria Eng. J.*, **54**(4), pp. 955–971.
- [35] Guo, Z., Zheng, C., and Shi, B., 2002, "Discrete Lattice Effects on the Forcing Term in the Lattice Boltzmann Method," *Phys. Rev. E - Stat. Nonlinear, Soft Matter Phys.*, **65**(4), pp. 1–6.
- [36] Ginzburg, I., 2005, "Generic Boundary Conditions for Lattice Boltzmann Models and Their Application to Advection and Anisotropic Dispersion Equations," *Adv. Water Resour.*, **28**(11), pp. 1196–1216.
- [37] Zhang, T., Shi, B., Guo, Z., Chai, Z., and Lu, J., 2012, "General Bounce-Back Scheme for Concentration Boundary Condition in the Lattice-Boltzmann Method," *Phys. Rev. E - Stat. Nonlinear, Soft Matter Phys.*, **85**(1), pp. 1–14.
- [38] Chen, Q., Zhang, X., and Zhang, J., 2013, "Improved Treatments for General Boundary Conditions in the Lattice Boltzmann Method for Convection-Diffusion and Heat Transfer Processes," *Phys. Rev. E*, **88**(3), p. 33304.
- [39] www.openphase.de, 2017, "OpenPhase," <http://www.openphase.de/> [Online]. Available: <http://www.openphase.de/>.
- [40] Dagum, L., and Menon, R., 1998, "OpenMP: An Industry Standard API for Shared-Memory Programming," *IEEE Comput. Sci. Eng.*, **5**(1), pp. 46–55.
- [41] Holdych, D. J., Noble, D. R., Georgiadis, J. G., and Buckius, R. O., 2004, "Truncation Error Analysis of

Lattice Boltzmann Methods,” J. Comput. Phys., **193**(2), pp. 595–619.